

Core-Shell DNA-Cholesterol Nanoparticles Exert Lysosomolytic Activity in African Trypanosomes**

Robert Knieß^{+, [a]} Wolf-Matthias Leeder^{+, [a]} Paul Reißig,^[a] Felix Klaus Geyer,^[a] and H. Ulrich Göringer^{*[a]}

Trypanosoma brucei is the causal infectious agent of African trypanosomiasis in humans and Nagana in livestock. Both diseases are currently treated with a small number of chemotherapeutics, which are hampered by a variety of limitations reaching from efficacy and toxicity complications to drug-resistance problems. Here, we explore the forward design of a new class of synthetic trypanocides based on nanostructured, core-shell DNA-lipid particles. In aqueous solution, the particles self-assemble into micelle-type structures consisting of a solvent-exposed, hydrophilic DNA shell and a hydrophobic lipid core. DNA-lipid nanoparticles have membrane-adhesive qual-

ities and can permeabilize lipid membranes. We report the synthesis of DNA-cholesterol nanoparticles, which specifically subvert the membrane integrity of the *T. brucei* lysosome, killing the parasite with nanomolar potencies. Furthermore, we provide an example of the programmability of the nanoparticles. By functionalizing the DNA shell with a spliced leader (SL)-RNA-specific DNAzyme, we target a second trypanosome-specific pathway (dual-target approach). The DNAzyme provides a backup to counteract the recovery of compromised parasites, which reduces the risk of developing drug resistance.

Introduction

The inherent complexity of developing, testing, and synthesizing new anti-infectives and therapeutics has never been more obvious than during the SARS-CoV2 pandemic. While modern-era drug development has benefitted immensely from the large amount of genome, proteome, and high-throughput data, the need for new and improved antiviral, antibacterial, antifungal, and antiparasitic medications has not vanished, and the search for alternative drug concepts and new drug targets has remained a key challenge in academic and industrial pharmaceutical research alike. This is especially the case for illnesses with unmet medical and therapeutic needs such as neglected tropical diseases (NTDs)^[1,2] including onchocerciasis, schistosomiasis, lymphatic filariasis, and human African trypanosomiasis (HAT). HAT, also known as African sleeping sickness, is caused by the two protozoan parasite species, *Trypanosoma brucei rhodesiense* and *Trypanosoma brucei gambiense*. While the incidence of HAT is currently at an unprecedented low,^[3] large


parts of Africa are still threatened by the disease.^[4] This is further aggravated by the zoonotic trypanosome species *T. congolense*, *T. vivax*, and *T. brucei brucei*, which thwart almost every agricultural progress in sub-Saharan Africa. HAT is fatal if left untreated, and due to the variable glycoprotein surface (VSG) of the parasite, all vaccination efforts have failed. As a consequence, the disease is treated by chemotherapy.^[5] Unfortunately, only a small number of clinically relevant compounds are available and these compounds suffer in part from grave side effects, narrow therapeutic windows, and the problem of parenteral administration. The situation is further vexed by the occurrence of treatment failures due to the rise of drug-resistant parasite strains.^[6] Consequently, despite the recent addition of fexinidazole as the first oral monotherapy against *T. b. gambiense* infections,^[5,7] new and improved drugs are still needed for the treatment of HAT.


Here, we present an alternative drug development concept, which we term dual-target approach (Figure 1). The method specifically aims to reduce the incidence of drug resistance by targeting two parasite-specific biochemical pathways simultaneously. As the first target, we focus on the lysosomal membrane of *T. brucei*. Lipid membranes represent a core characteristic in all living systems, and multiple synthetic and biological compounds capable of disrupting lipid membranes have been identified.^[8] The heightened vulnerability of *T. brucei* to the destruction of the lysosome is demonstrated by the action of the naturally evolved trypanolytic factors TLF-1 and TLF-2.^[9] Both factors are high molecular mass human serum components, which cause non-human infectious trypanosomes to lyse. The lytic ingredient in both complexes is apolipoprotein L1 (APOL1). APOL1 is a Bcl-2-like protein that upon acidification forms pores in the lysosomal membrane, which allows the influx of chloride anions and H₂O resulting in the uncontrolled osmotic swelling of the lysosome, ultimately destroying the

[a] Dr. R. Knieß,⁺ Dr. W.-M. Leeder,⁺ P. Reißig, F. K. Geyer, Prof. Dr. H. U. Göringer
Molecular Genetics
Technical University Darmstadt
Schnittspahnstr. 10, 64287 Darmstadt (Germany)
E-mail: goringer@bio.tu-darmstadt.de

[⁺] These authors contributed equally to this work.

[**] A previous version of this manuscript has been deposited on a preprint server (<https://doi.org/10.1101/2022.07.18.500428>).

 Supporting information for this article is available on the WWW under <https://doi.org/10.1002/cbic.202200410>

 © 2022 The Authors. ChemBioChem published by Wiley-VCH GmbH. This is an open access article under the terms of the Creative Commons Attribution Non-Commercial NoDerivs License, which permits use and distribution in any medium, provided the original work is properly cited, the use is non-commercial and no modifications or adaptations are made.

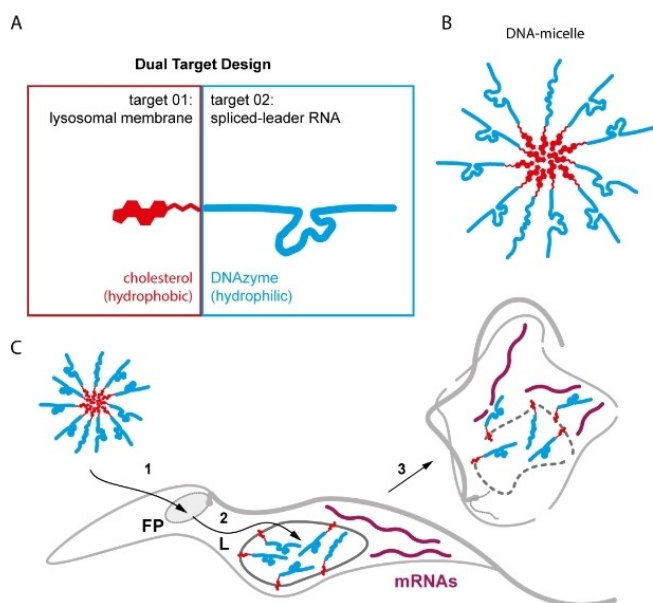


Figure 1. Design of core-shell forming DNA-cholesterol conjugates targeting two parasite-specific pathways (dual-target approach). (A) Bipartite domain structure of a cholesterol-modified oligodeoxyribonucleotide that targets the lysosomal membrane (target-1) and the spliced leader (SL)-RNA (target-2) of African trypanosomes. Target-1 is tackled by the cholesterol moiety (sterol scaffold in red) and target-2 is attacked by an RNA-cleaving DNAzyme (cyan). (B) Core-shell nanoparticles self-assemble in aqueous solution resulting in micelle-type high-molecular-mass particles. Red: hydrophobic cholesterol core. Cyan: hydrophilic DNAzyme shell. (C) Putative uptake pathway of the DNAzyme-cholesterol nanoparticles by infective stage trypanosomes. 1: Binding and internalization through the flagellar pocket (FP). 2: Endosomal routing to the lysosome (L). 3: Interaction with the inner lysosomal membrane causes the lysosome to collapse. Escaping DNAzyme-cholesterol molecules catalyze the breakdown of cytosolic mRNAs (purple).

parasite. Disruption of the lysosome as a trypanocidal principle has been demonstrated for a diverse group of reagents, including neuroendocrine peptides,^[10] L-leucyl-L-leucyl methyl ester,^[11,12] and different synthetic triterpenoid-peptide conjugates.^[13] As the second target, we chose the spliced leader (SL)-RNA of *T. brucei*. The 39nt long RNA sequence is the result of a *trans*-splicing reaction and it constitutes the 5'-end of every *T. brucei* mRNA.^[14] SL-RNA addition generates monocistronic mRNAs from polycistronic primary transcripts and provides every transcript with a 5'-Cap structure. As such, the reaction is required for the formation of translation-competent mRNAs and, therefore, it is essential. This is further evidenced by the fact that extreme stress conditions result in a complete shut-down of SL-RNA transcription, a phenomenon known as spliced leader silencing (SLS).^[15,16] Moreover, acridine-derivatized SL-RNA-specific antisense oligodeoxynucleotides have been shown to kill *T. brucei* in cell culture.^[17,18]

For the synthesis of a lysosomolytic and at the same time SL-RNA-cleaving reagent, we utilize the well-established technology of core-shell DNA-lipid nanostructures.^[19–21] Derivatizing oligodeoxynucleotides with hydrophobic side chains such as alkyl groups, tocopherol, porphyrins, or cholesterol generates DNA-amphiphiles that self-assemble into macromolecular micelle-type particles. DNA-lipid nanoparticles consist of a mem-

brane-adhesive core and a hydrophilic DNA shell (Figure 1A,B), which are capable of binding and disrupting lipid bilayers. They have been used for pore formation and drug delivery purposes,^[20,22,23] and specifically cholesterol-derivatized DNA nanoparticles have been applied to functionalize the surface of liposomes, form membrane-spanning pores, and induce membrane curvature and tubulations.^[24–26] Even though cholesterol is considered a rigid membrane lipid, the molecule can adopt numerous conformations due to the asymmetry of the sterane backbone and the inherent flexibility of the isooctyl side chain. This can generate lipid bilayers with spatially altered biomechanical properties, which as a consequence can perturb the local membrane integrity.^[27,28] A further advantage of DNA-lipid nanoparticles is their programmability. The molecules can be engineered for specific applications by using DNA sequences that execute defined functions.^[19] Here, we report the synthesis of DNA-lipid nanoparticles consisting of a SL-RNA-specific deoxyribozyme (DNAzyme) covalently attached to a cholesterol group. The construct challenges two essential parasite-specific pathways: the spliced leader sequence at the 5'-end of every *T. brucei* mRNA and the membrane integrity of the parasite lysosome (Figure 1C). We demonstrate nanoparticle formation of the synthesized conjugates and verify that the DNAzyme is enzymatically active within the micellar context. Upon incubation with infective-stage trypanosomes, we show uptake and routing of the particles to the lysosome followed by lysosomal collapse and cell death. As such, we provide evidence for the forward design of a synthetic DNA-lipid nanostructure with therapeutic potential for the treatment of African trypanosomiasis.

Results and Discussion

Synthesis of SL-DNAzyme-cholesterol conjugates

SL-RNA-cleaving DNAzyme-cholesterol conjugates were synthesized by automated oligonucleotide synthesis using standard phosphoramidite chemistry. The DNAzyme is 39nt in length and consists of a 13nt 8–17-type DNAzyme core domain^[29,30] flanked by two 12 and 14nt long single-stranded (ss) extensions. The ss-sequences provide base complementarity to the *T. brucei* SL-RNA and position the catalytic core of the DNAzyme to cleave the ribose-phosphate backbone between nucleotides G14 and A15 (Figure 2A). Conjugation of the cholesterol moiety was performed co-synthetically either at the 5'- or 3'-end of the DNAzyme using tetraethylglycol (TEG) or prolinol (Pro) linker chemistries (Figure 2B). Control oligodeoxynucleotides were synthesized without cholesterol and with 5'-stearyl or 5'-oleate residues replacing cholesterol (Figure 2B). Synthesis products were purified by reversed-phase HPLC to purities $\geq 97\%$ (Supporting Information Figure S1) and were confirmed by mass spectrometry. A complete list of all synthesized oligonucleotide-conjugates is provided in Supporting Information Table S1.

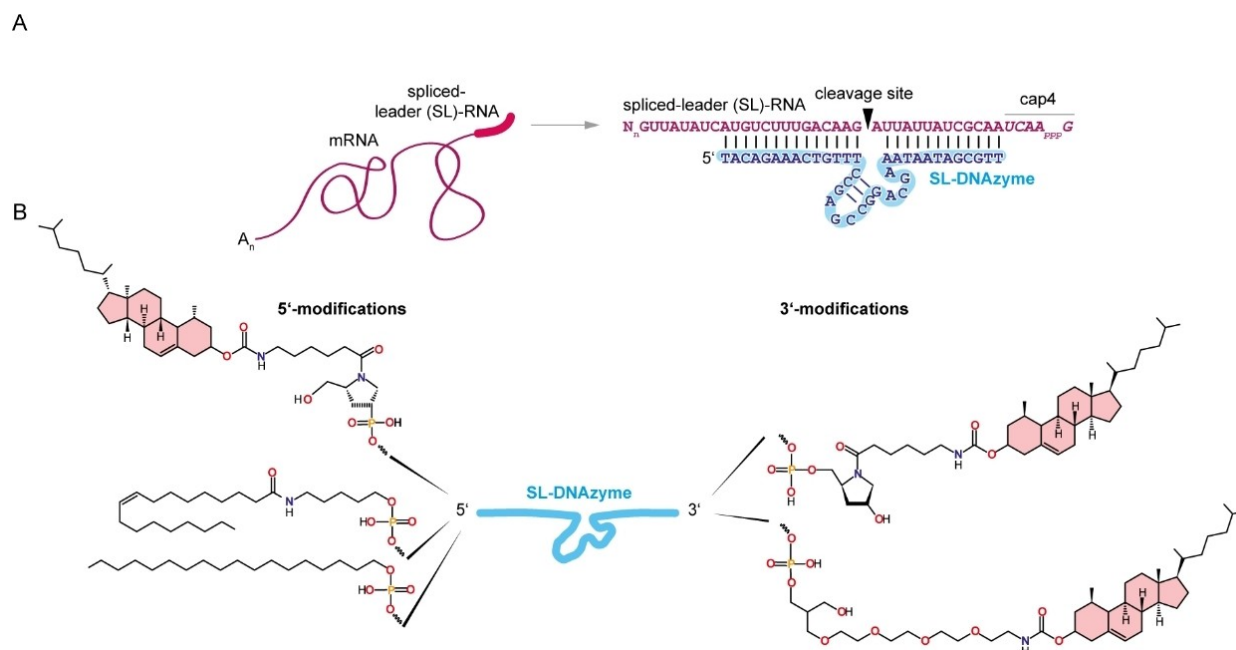


Figure 2. (A) Left: Sketch of a *trans*-spliced and poly-adenylated *T. brucei* mRNA (purple). Right: Nucleotide sequence and base-pairing of a spliced-leader (SL)-RNA/DNAzyme hybrid. Purple: SL-RNA. Cyan: SL-DNAzyme. The SL-RNA is 39nt long and carries a hypermethylated cap4-structure. The scissile phosphodiester bond is marked by an arrowhead. (B) Summary of the different end-modifications of the SL-DNAzyme. 5'-end modifications (top to bottom): prolinol (Pro)-cholesterol, C₆-oleate, stearyl. 3'-end modifications (top to bottom): Pro-cholesterol, tetraethylene glycol (TEG)-cholesterol. The cholesterol scaffold is colored in red.

Formation of high molecular mass core-shell nanoparticles

DNA-amphiphiles in aqueous solution self-assemble into high molecular mass core-shell particles.^[19,20] The reaction is entropically driven and was experimentally confirmed by isokinetic ultracentrifugation in glycerol gradients. Figure 3A shows a representative result using the SL-DNAzyme 3'-cholesterol conjugate. The molecule assembles into nanoparticles with an apparent *S*-value of $13S \pm 3S$, which calculates to an apparent molecular mass of approximately 450 kDa and an apparent aggregation number (N_{agg}) of 39 monomers/micelle. Figure 3B shows a visualization of the formed micelles using atomic force microscopy (AFM). The sample shows a monodisperse distribution of globular particles ranging from 13 to 23 nm in diameter with a mean of 18 nm. A further visualization was achieved by gel electrophoresis in native, high-percentage agarose gels (Figure 3C and Supporting Information Figure S2). As expected, the different DNAzyme-cholesterol constructs migrate as high molecular mass complexes with apparent sizes between 400 and 530 kDa. This enumerates to a mean apparent N_{agg} of 44 molecules/micelle confirming the N_{agg} -measurement by isokinetic ultracentrifugation. Lastly, we measured the critical micelle concentration (CMC) for each of the DNA-cholesterol constructs. For that, we relied on the solvatochromic properties of the benzophenoxazine dye Nile red.^[31] Figure 3D shows the SL-DNAzyme-3'-cholesterol micelle as an example. The molecule has a CMC of 42 nM. The CMCs for all DNA-micelle constructs range from 13 to 116 nM with a mean of 71 nM, which is in agreement with published values, varying between 10–

100 nM.^[32–36] Importantly, the stearate- and oleate-substituted constructs do not form nanoparticles at concentrations $\leq 3 \mu\text{M}$ (Supporting Information Table S1).

SL-DNAzyme-cholesterol nanoparticles are catalytically active

The enzymatic activity of the SL-DNAzyme was analyzed *in vitro*. For that, we synthesized a 5'-Cy5-modified SL-DNAzyme and a 5'-FAM-derivatized SL-RNA model substrate. The RNA consists of the first 27nt of the *T. brucei* SL-RNA sequence (Figure 4A) with a single AG-dinucleotide at positions 13/14. Different fluorophores were used for the DNAzyme and the substrate RNA to monitor the two reactants independently by laser-induced fluorescence (LIF). Since the 8–17 DNAzyme is a metalloenzyme, reactions were started by the addition of Mn^{2+} . As shown in Figure 4B the SL-oligoribonucleotide is precisely cleaved at the targeted AG-dinucleotide, generating the predicted 13nt long FAM-labeled 5'-cleavage product and as expected for an enzyme, the SL-DNAzyme remains unaltered during the catalytic conversion. Next, we analyzed whether the RNA cleavage reaction can be performed in the context of the DNAzyme-cholesterol nanoparticle (Figure 4C). For that, we used the SL-DNAzyme-3'-cholesterol construct as a representative. Figure 4D shows the cleavage reaction of the SL-oligoribonucleotide at single turnover conditions over a period of 3 h. The micelle-embedded DNAzyme cleaves the SL-RNA oligonucleotide with a k_{cat} of 0.01/min and processes up to 75% of the input. This is identical to the non-substituted, free SL-

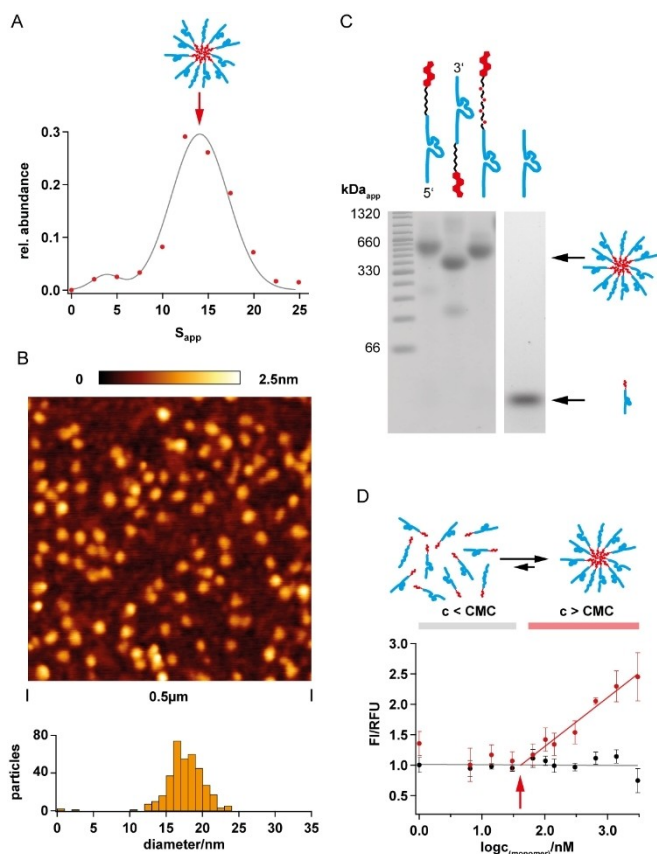


Figure 3. (A) Sedimentation profile of a SL-DNAzyme-cholesterol nanoparticle in a linear 10–35% (v/v) glycerol gradient. The particle sediments with an apparent S -value (S_{app}) of $13 \pm 3S$. (B) Atomic force microscopy (AFM) of SL-DNAzyme-cholesterol nanoparticles on a mica surface. The dried micelles vary in diameter between 13 and 23 nm with a mean of 18 nm. (C) Electrophoretic separation of different DNAzyme-cholesterol nanoparticles in non-denaturing 3% (w/v) agarose gels (for a summary of the molecule drawings see Supporting Information Table S1). The different conjugates migrate with apparent molecular sizes between 400 and 530 kDa. (D) CMC measurement of an SL-DNAzyme-cholesterol conjugate using the solvatochromic fluorogenic dye 9-(diethylamino)-5*H*-benzo[*a*]phenoxazin-5-one (Nile red). A list of all measured CMC values is given in Supporting Information Table S1. FI = fluorescence intensity. RFU = relative fluorescence unit.

DNAzyme, indicating that the molecule is fully accessible within the micellar assembly (Supporting Information Figure S3). Importantly, the nanoparticles are also active under multiple turnover conditions (Figure 4E). At a 10x, 15x, and 30x molar excess of SL-RNA over DNAzyme we measured k_{cat} values between 0.015 and 0.04/min with up to 95% substrate conversion. Lastly, we determined that the micelle-embedded SL-DNAzyme is active at temperatures between 10 °C and 42 °C, at pH values between 6.8 to 8.8, and that Mn^{2+} can be replaced by Co^{2+} , Ca^{2+} , and Mg^{2+} (Supporting Information Figure S3).

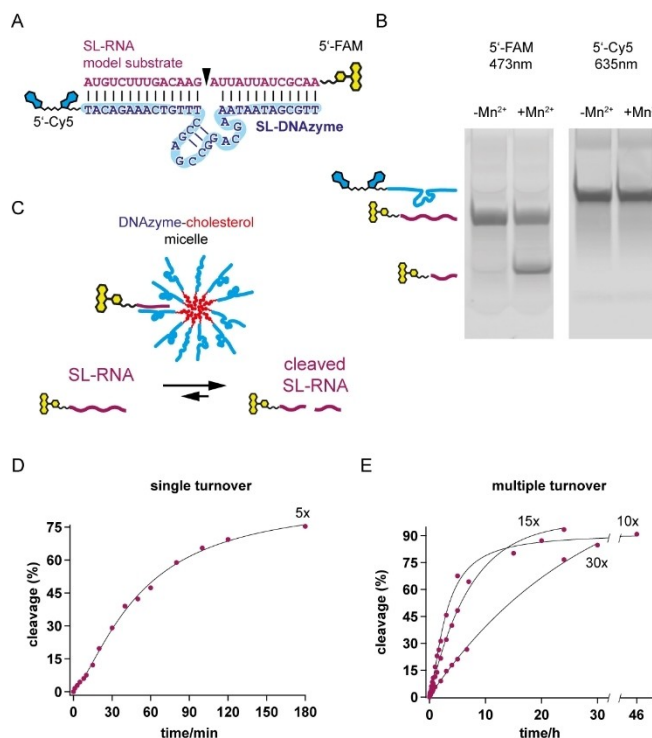


Figure 4. (A) Sequence outline of the SL-DNAzyme/SL-RNA enzyme-substrate complex (DNAzyme = cyan; SL-RNA = purple). The SL-RNA mimicking oligonucleotide is 5'-FAM-labeled (fluorescein scaffold in yellow) and the SL-DNAzyme is 5'-Cy5-modified (cyanine scaffold in blue). The catalytic center of the DNAzyme consists of a short hairpin next to four single-stranded nt (ACGA). The RNA cleavage site is an AG-dinucleotide (arrowhead). (B) Representative gel-electrophoretic result of an RNA-cleavage assay in the presence (+) and absence (-) of Mn^{2+} . The input SL-RNA oligonucleotide, the 5'-cleavage product, and the SL-DNAzyme are separated in a denaturing polyacrylamide gel followed by LIF-detection at 473 nm (FAM) and 635 nm (Cy5). The cleavage reaction is Mn^{2+} -dependent; as expected, the DNAzyme leaves the reaction unaltered. (C) Graphical outline of the DNAzyme-mediated SL-RNA cleavage reaction in the context of the assembled core-shell nanoparticle. (D) Single turnover kinetic of a SL-RNA cleavage reaction by a SL-DNAzyme-cholesterol nanoparticle at a 5x molar excess of SL-DNAzyme over SL-RNA substrate. Up to 75% of the input SL-RNA is cleaved after 3 hours. (E) The same analysis as in (D) under multiple turnover conditions (10x, 15x, 30x molar excess of SL-RNA over SL-DNAzyme). RNA substrate conversions of up to 90% are achieved.

SL-DNAzyme cholesterol nanoparticles kill bloodstream-stage trypanosomes

The trypanocidal activity of the different SL-DNAzyme-cholesterol micelles was tested by incubating infective-stage trypanosomes with increasing concentrations (0–320 nM) of the nanoparticle constructs. Parasite survival was measured in a live cell assay, based on the cleavage of the membrane-penetrating, fluorogenic calcein-acetoxymethyl (AM) ester by intracellular esterases.^[37,38] As shown in Figures 5A and B (and Supporting Information Figure S4), all DNA-micelle variants act as potent trypanocidals. Half-maximal lethal concentrations (LC_{50}) range from 33 to 79 nM for the different constructs (Figure 5B) and the trypanocidal activity is neither influenced by the linker chemistry (prolinol or TEG) nor by the 5'- or 3'-positioning of the cholesterol moiety. The killing reaction (at $5xLC_{50}$) reaches

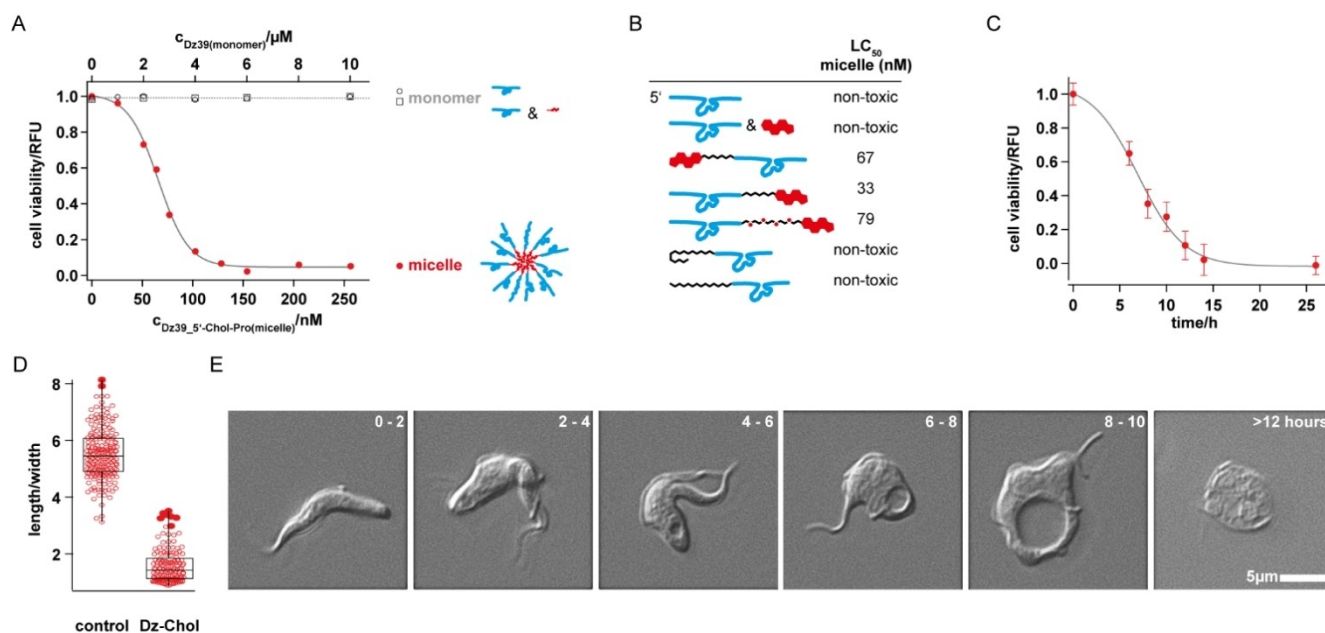


Figure 5. Cell viability analysis. (A) Dose-response curves of infective-stage trypanosomes treated with SL-DNAzyme-cholesterol nanoparticles (filled circles, red), non-conjugated SL-DNAzyme (open circles, black), and non-conjugated SL-DNAzyme in the presence of saturating amounts of free cholesterol (open squares, black). RFU = relative fluorescence unit. (B) Summary of the derived half-maximal lethal concentrations (LC_{50}) for the different nanoparticles. Top to bottom: non-conjugated SL-DNAzyme, non-conjugated SL-DNAzyme in the presence of saturating amounts of cholesterol, 5'-Chol-pro-SL-DNAzyme, SL-DNAzyme-3'-pro-Chol, SL-DNAzyme-3'-TEG-Chol, 5'-oleate-SL-DNAzyme, and 5'-stearyl-SL-DNAzyme. For a summary of the molecule drawings see Supporting Information Table S1. (C) Cell viability kinetic of infective-stage trypanosomes treated with SL-DNAzyme-cholesterol nanoparticles ($8 \times LC_{50}$). The half-maximal survival time is 7.0 ± 0.8 h. Errors are standard deviations. (D) Box plot analysis of the length/width ratio of infective-stage trypanosomes treated with non-conjugated SL-DNAzyme ($c = 10 \mu\text{M}$) and SL-DNAzyme-cholesterol nanoparticles (DzChol $c = 8 \times LC_{50}$). The median length/width ratio changes from 5.4 to 1.4. Incubation time = 8 h. (E) Representative DIC microscopy images of infective-stage trypanosomes treated with SL-DNAzyme-cholesterol nanoparticles ($8 \times LC_{50}$) for 0 to > 12 h as indicated. For a time-lapse movie of the process, see Supporting Information Video S1.

> 95% completion after 13 hours, which roughly represents two parasite cell doublings (Figure 5C). Importantly, the unmodified SL-DNAzyme shows no inhibitory activity even in the presence of saturating amounts (67 nM) of free cholesterol (Figure 5A).^[39] Similarly, the DNA-oleate and DNA-stearate constructs do not have trypanocidal activity (Figure 5B). Also, insect-stage trypanosomes were shown to be unaffected even at concentrations ≥ 5 -fold the LC_{50} . This suggests a specificity for the infective, bloodstream-stage of the parasite.

Figure 5E and Supporting Information Video S1 show differential interference contrast (DIC) microscopic images of individual DNAzyme-cholesterol nanoparticle-treated *T. brucei* cells. Starting at 2 h of incubation, the parasites lose their characteristic slender shape and adopt an enlarged and bloated morphology. This coincides with the appearance of a vacuolar substructure, which increases until it dominates the cell body at 8–10 h of incubation. At this stage, the median length/width ratio of the cells has changed from 5.6 to 1.4 (Figure 5D). Further incubation (> 12 h) results in a complete loss of the trypanosome cell shape, the appearance of intracellular granules, and finally cell lysis.

Using FITC-labelled dextran as a fluid phase marker, we identified the vacuolar substructure as the lysosome. FITC-dextran is endocytotically taken up and routed to the lysosome.^[40] As shown in Figure 6A, parasites treated with DNAzyme nanoparticles (for 6–8 h) show a perfect overlap of

the fluorescent FITC-dextran signal in the lysosome with the large vacuole. This was further confirmed by directly labeling the DNAzyme micelles with 6-carboxyfluorescein (6-FAM) (Figure 6B). As before, at early incubation times (2–4 h) the 6-FAM signal perfectly localizes to the lysosome. At 8–10 h the signal in the lysosomal lumen diminishes and staining of the lysosomal membrane, the cytosol and the inner plasma membrane is detected. At 10–12 h, the lysosomal signal disappears and spreads out through the entire cell, indicating the collapse of the lysosomal membrane. At > 12 h, the cells have lost all subcellular structure, and fluorescence is distributed throughout the cytosol, with some punctate signals likely representing stained membrane fragments. Different from the synthetic trypanolytic factor synTLF,^[13] the nucleus and kinetoplast of the nanoparticle-treated parasites are not affected (Figure 6A,B).

A functional DNAzyme is not required for the trypanocidal effect

Lastly, we tested whether the trypanolytic activity of the DNAzyme nanoparticles is driven by the cholesterol-mediated collapse of the lysosome, or by the DNAzyme-guided cleavage of the SL-RNA sequence, or both. For that, we synthesized a series of nanoparticle constructs with shortened DNAzyme

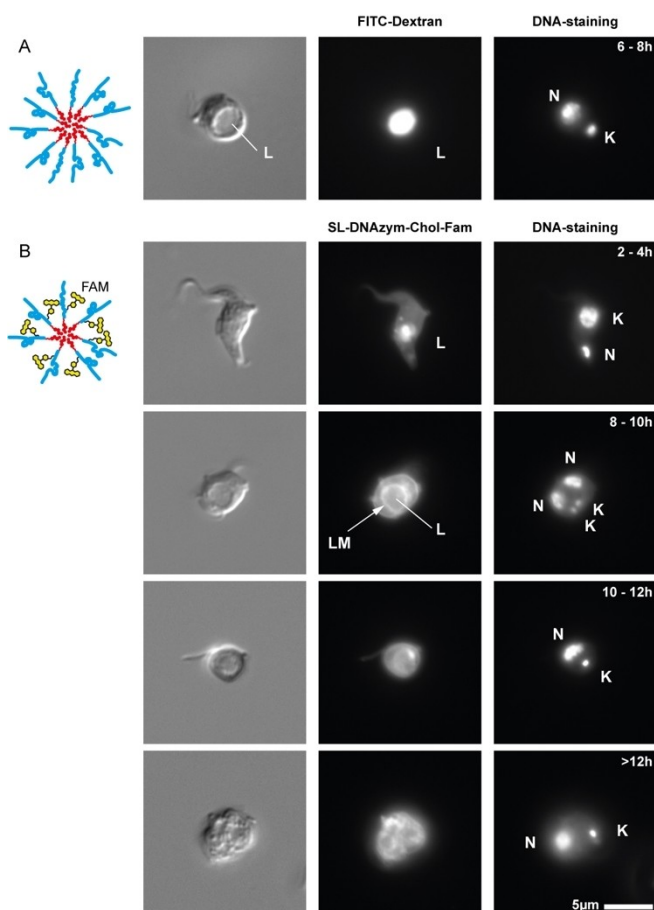


Figure 6. Intracellular localization and fate of the SL-DNAzyme-cholesterol nanoparticles. Left panels: Differential interference contrast (DIC) imaging. Center panels: Fluorescence imaging (FITC and FAM). Right panels: DNA staining. N = nuclear DNA. K = kinetoplast DNA. (A) Visualization of the lysosome (L) using FITC-labeled dextran. (B) Intracellular localization of a FAM-labeled SL-DNAzyme-cholesterol nanoparticle (FAM-DzChol) between 2 and > 12 h of incubation. LM = lysosomal membrane. For a time point < 2 h see Supporting Information Figure S5.

sequences 31, 20, 10, and 6nt in length. Except for the 31nt long DNA, none of the truncated sequences can fold into a catalytically active DNAzyme. Nevertheless, all constructs show trypanolytic activity (Figure 7A and Supporting Information Table S1), proving that the enzymatic activity of the DNAzyme is neither necessary nor sufficient for the trypanolytic effect. LC_{50} -values range from 62 to 182 nM with an inverse linear relationship between nt-length and LC_{50} (Figure 7B). Further support was gained from the synthesis of a DNA nanoparticle with a randomized 39nt non-DNAzyme sequence. As anticipated the construct displays an LC_{50} of 51 nM (Figure 7A), almost identical to the 39nt SL-DNAzyme nanoparticle (LC_{50} = 33–67 nM). We also established that RNA-based nanoparticles, as well as nuclease-resistant, phosphorothioate-modified DNA sequences, function as trypanocides (Supporting Information Table S1). This demonstrates a high sequence and length plasticity of the nucleic acid domain of the nanoparticles (for a summary see Supporting Information Figure S6) and establishes that only the membrane fenestration step is necessary and

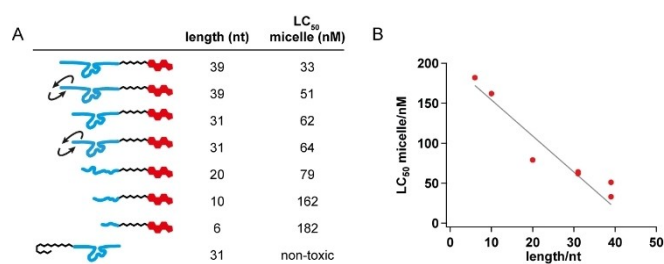


Figure 7. Nucleotide length analysis. (A) LC_{50} -values of different DNA-cholesterol constructs ranging from 39nt to 6nt. The different conjugates are depicted as cartoons with the DNA domain in cyan and the cholesterol moiety in red. For a summary of the molecule drawings see Supporting Information Table S1. DNA molecules < 31nt cannot adopt a functional DNAzyme fold. (B) Nucleotide length-dependency of the measured LC_{50} -values. The data are correlated with a Pearson's $r = -0.965$.

sufficient for the trypanocidal effect. It further indicates a sequence-independent role for the DNA shell in the process, possibly contributing to the parasite binding and internalization steps. This is supported by the fact that trypanosomes are deficient in the *de novo* synthesis of purines. The parasites rely on the receptor-mediated uptake of free purines and purine nucleosides,^[41,42] and short DNA and RNA oligonucleotides have also been shown to be internalized.^[17,18,43–45] As such it is feasible that the DNA shell, at least in part, acts as the nanoparticle haptophore.

Mode-of-action

Together, our results are suggestive of the following mode-of-action (MOA) for the DNA-cholesterol nanoparticles. Upon incubation with infective-stage trypanosomes, the particles bind to the flagellar pocket of the parasite. The FP is a highly specialized area on the surface of the parasite, which executes all endo- and exocytotic processes. Since trypanosomes rely on the efficient recycling of their protein surface coat, the FP is connected to a rapid and highly effective vesicular routing system,^[46] which transports the nanoparticles to the lysosome. Within the lysosome, the DNA-nanoparticles execute a membrane-destabilizing effect that causes the lysosome to collapse (Figure 8). This ultimately kills the cells. Importantly, only covalently connected DNA-cholesterol constructs execute the lysosomolytic activity. Neither DNA alone nor cholesterol alone nor a mixture of both molecules is cytotoxic. Furthermore, the trypanocidal effect is strictly dependent on the cholesterol core of the nanoparticles. Cholesterol cannot be substituted by other fatty acids, such as oleate or stearate, which likely are not internalized efficiently. However, the DNA shell adds to the toxophore properties of the particles as well. DNA-cholesterol nanoparticles have been shown to adsorb to lipid membranes by ionic contacts..^[47,48] This is mediated by the polyanionic surface charge of the DNA shell and therefore it is plausible that DNA sequences with a length of 39nt show a higher lysosomolytic potency than shorter oligodeoxynucleotides (Figure 7B). The charge/charge-based membrane/DNA interaction

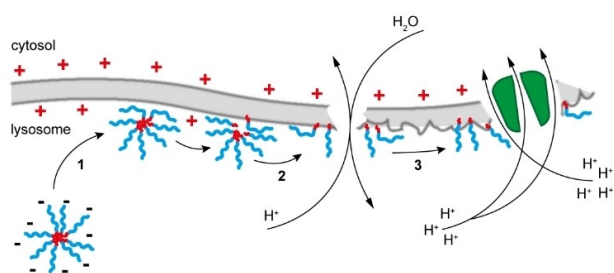


Figure 8. Mechanistic model of the DNA nanoparticle/lipid membrane interaction inside the *T. brucei* lysosome. Step 1: Electrostatic binding of the polyanionic DNA shell to the inner lysosomal membrane. Step 2: Destabilization of the DNA shell and membrane integration of the hydrophobic cholesterol molecules. Step 3: The accumulation of cholesterol molecules in the luminal leaflet of the lysosome generates an asymmetric/dysfunctional membrane architecture. This causes the leakage of protons into the cytosol and the influx of water into the lysosome. Lysosomal swelling and disruption of the membrane ultimately kill the parasite.

draws the cholesterol core to the lysosomal membrane (Figure 8) where the molecules integrate into the inner leaflet of the membrane.^[19,24,49] This generates a highly asymmetric lipid bilayer and as a result skews the biomechanical properties of the lysosomal membrane.^[50–52] The massive enlargement of the lysosome and the subsequent osmotic swelling of the parasite are testament of the compromised membrane integrity^[53,54] as is the observed leakage of FITC-dextran from the lysosome into the cytosol after > 8 h of incubation. Ultimately, as designed, large-scale lysosomal membrane failure, fragmentation of the organelle itself, and fenestration of other membrane compartments kill the parasite. As such, the MOA is qualitatively similar to the lysosome-associated defects caused by the natural trypanolytic serum factors TLF1 and TLF2^[55,56] and the synthetic trypanolytic factor synTLF.^[13] Quantitatively, however, DNA-cholesterol nanoparticles exhibit half-maximal lethal concentrations as low as 0.033 μM , which is about one order of magnitude lower compared to recombinant APOL1 (0.23 μM)^[56] and about 100 times lower than synTLF (3 μM).^[13]

Lastly, it is important to note that the in-built DNAzyme activity of the nanoparticles, targeting the 5'-end of every *T. brucei* mRNA is dispensable for the trypanocidal effect. DNA-cholesterol nanoparticles with truncated or non-DNAzyme sequences elicit the same cytotoxicity as particles that include the DNAzyme sequence. However, we cannot exclude that the DNAzyme activity is masked by the dominant outcome of the lysosomal membrane collapse, and in that case, the SL-DNAzyme activity can provide a backup MOA to counteract the recovery of compromised parasite cells.

Conclusion

In summary, we have demonstrated the rational design of nanostructured DNA-cholesterol amphiphiles with therapeutic potential for the treatment of African sleeping sickness. The molecules are specific for the infective lifecycle stage of trypanosomes and kill the parasite at nanomolar concentrations

(30 nM). At this concentration, the amphiphiles form high molecular mass, micelle-type nanoparticles (450 kDa, 13S), which consist of a hydrophilic solvent-facing DNA shell and a hydrophobic cholesterol core. The trypanocidal activity of the particles resides in the cholesterol core. The lipid molecules destabilize the lysosomal membrane, which eventually generates an autophagy-like phenotype. In addition, we demonstrated that the DNA shell can be functionalized for instance with a SL-RNA-specific DNAzyme. This can provide a backup mode-of-action to reduce the risk of developing drug resistance.

Experimental Section

Growth of trypanosome cells: The bloodstream life cycle stage of *Trypanosome brucei brucei* strain Lister 427 (MITat serodeme, variant clone MITat 1.2) was grown in HMI-9 medium^[57] supplemented with 10% (v/v) heat-inactivated fetal calf serum (FCS), 0.2 mM 2-mercaptoethanol and 100 U/mL penicillin/streptomycin (Gibco™ Thermo Fisher Scientific). Parasites were grown at 37 °C in 95% air, and 5% CO₂ at a relative humidity (rH) \geq 95%. Insect-stage (procyclic) parasites were grown at 27 °C in SDM-79 medium as described.^[58] Parasite cell densities were determined by automated cell counting.

Synthesis of cholesterol-modified DNA-oligonucleotides: Cholesterol-modified oligodeoxynucleotides were synthesized by automated solid-state synthesis on controlled pore glass (CPG)-beads (200nmol synthesis scale) using 5'-dimethoxytrityl-2'-deoxy,3'-[(2-cyanoethyl)-(N,N-diisopropyl)]-phosphoramidites. Cholesteryl moieties were co-synthetically introduced either at the 5'- or 3'-ends of the different oligonucleotides using tetraethylene glycol (TEG) or prolinol (Pro) linker chemistries. Control oligonucleotides were synthesized with 5'-stearyl or 5'-oleate modifications, with backbone phosphorothioate (PTO) modifications, and with a 6-Carboxyfluorescein (6-FAM) fluorescence tag. In addition, an "all-RNA" variant was synthesized using 2'-O-tert-butyl dimethylsilyl (TBDMS)-protected phosphoramidites. The crude synthesis products were purified by reverse phase high-performance liquid chromatography (RP-HPLC), analyzed by mass spectrometry (MALDI-TOF), and further scrutinized in 8 M urea-containing, 18% (w/v) polyacrylamide gels (Supporting Information Figure S1). Concentrations were derived from UV-absorbency measurements at 260 nm (A_{260}) using the molar extinction coefficients (ϵ in L/mol \times cm) listed below. The following oligonucleotide sequences were synthesized:

Dz39_5'-Chol-Pro: Chol-Pro-TACAGAACTGTTCCGAGCCGGAC-GAAATAATAGCGTT (448300)

Dz39_3'-Chol-Pro: TACAGAACTGTTCCGAGCCGGACGAAATAATAGCGTT-Pro-Chol (448300)

Dz39_3'-Chol-TEG: TACAGAACTGTTCCGAGCCGGACGAAATAATAGCGTT-TEG-Chol (448300)

Dz39: TACAGAACTGTTCCGAGCCGGACGAAATAATAGCGTT (448300)

D39rand_3'-Chol-Pro: AAATCCGAGATGTGAGGTTAATGCTCCAT-GAACGACATC-Pro-Chol (448300)

Dz31_5'-Chol-Pro: Chol-Pro-GAACTGTTCCGAGCCGGACGAAATAATAG (363200)

Dz31_3'-Chol-Pro: GAACTGTTCCGAGCCGGACGAAATAATAG-Pro-Chol (363200)

D31rev_3'-Chol-Pro: GATAATAAGCAGGCCGAGCCTTTGTCAAAG-Pro-Chol (363200)

Dz31_5'-Oleate: Oleate-C5-GAAACTGTTCCGAGCCGGACGAAATAA-TAG (363200)

Dz31_5'-Stearyl: Stearyl-GAAACTGTTCCGAGCCGGACGAAATAATAG (363200)

Dz31_5'-Chol-Pro-FAM: Chol-Pro-GAAACT*GTTCCGAGCCGGAC-GAAATAATAG (363200)

Dz31: GAAACTGTTCCGAGCCGGACGAAATAATAG (363200)

Dz31_5'-Cy5: Cy5-GAAACTGTTCCGAGCCGGACGAAATAATAG (383400)

D20_3'-Chol-Pro: AAATCCGAGATGTGAGGTTA-Pro-Chol (239000)

R20_3'-Chol-Pro: AAAUCCGAGAUGUGAGGUUA-Pro-Chol (239000)

D20PTO_3'-Chol-Pro: A*A*A*T*C*G*A*G*A*T*G*T*G*A*G*G*T*-T*A-Pro-Chol (239000)

D20: AAATCCGAGATGTGAGGTTA (239000)

D10_3'-Chol-Pro: ATGTGAGGTT-Pro-Chol (114400)

D10: ATGTGAGGTT (114400)

D6_3'-Chol-Pro: AAATCC-Pro-Chol (70400)

5'-FAM SL-RNA_21nt: FAM-CGCUAUUUAUAGAACAGUUUC (250200)

5'-FAM SL-RNA_27nt: FAM-AACGCUAUUUAUAGAACAGUUUCUGUA (326500)

Formation of DNA-cholesterol nanoparticles and CMC-determination: Cholesterol-modified oligonucleotides were solubilized in 10 mM Tris/HCl pH 7.5, 1 mM EDTA (TE)-buffer at a concentration of 0.1 mM. When aqueous buffer is added, micelles are formed by spontaneous self-association. Critical micelle concentrations (CMC) were determined as in [31]. For that the cholesterol-modified oligodeoxynucleotides were taken up in 25 mM 9-(diethylamino)-5*H*-benzo[*a*]phenoxazin-5-one (Nile red, C₂₀H₁₈N₂O₂) in anhydrous MeCN. Samples were incubated at 20 °C overnight followed by the stepwise addition of phosphate-buffered saline (PBS) pH 7.4 to a DNA-cholesterol monomer concentration of 3 μM. Dilutions for fluorescence measurements were made using freshly prepared 0.03 mM Nile red in PBS and measurements were performed in transparent, flat-bottom 96-well plates in a final volume of 0.1 mL. Fluorescence spectra (λ_{ex} 535 nm) were recorded in 2 nm steps in a TECAN Infinite 200PRO plate-reader. Relative fluorescent units (RFU) were integrated between 630 and 680 nm and the fluorescence intensities were normalized and plotted as a function of the concentration of DNA-cholesterol. Data points were subjected to a linear fit to calculate the CMC.

Sedimentation analysis of DNA-cholesterol nanoparticles: DNA-cholesterol micelles at ≥10xCMC were formed in 20 mM HEPES/KOH pH 7.5, 10 mM MgCl₂, 0.1 mM Na₂EDTA containing either 150 mM NaCl or 30 mM KCl. Samples were loaded onto 2 mL linear 10–35% (v/v) glycerol gradients and centrifuged at 20 °C for 155 min at 45,000 rpm in a Beckmann Coulter TLS55-rotor. Gradient fractions (0.2 mL) were EtOH-precipitated and the DNA-cholesterol material in each fraction was analyzed in denaturing (8 M urea), 18% (w/v) polyacrylamide gels. The gels were stained with Toluidine Blue O and densitometrically analyzed. Apparent sedimentation coefficients (S_{app}) and the corresponding apparent molecular masses (MW_{app}) of the nanoparticles were calculated from a non-linear fit of the sedimentation behavior of the following size standards: *E. coli* tRNA (4S, 2.8 × 10⁴ Da), *E. coli* 5S rRNA (5S, 4.2 × 10⁴ Da), *E. coli* 16S rRNA (16S, 5.4 × 10⁵ Da), *E. coli* 23S rRNA

(23S, 1 × 10⁶ Da), *T. brucei* CR4 pre-mRNA (9S, 1.6 × 10⁵ Da) and *T. brucei* Cyb pre-mRNA (14S, 4.3 × 10⁵ Da). Nanoparticle aggregation numbers (N_{agg}) were calculated as $N_{agg} = MW_{micelle} / MW_{monomer}$

Visualization of DNA-cholesterol nanoparticles: DNA-cholesterol micelles were electrophoretically separated in 3% (w/v) agarose gels in TBE pH 8.3 buffer (89 mM Tris-OH, 89 mM B(OH)₃, 2 mM EDTA) followed by staining with the fluorescent cyanine dye SYBR-gold (λ_{ex} 473 nm, λ_{em} 510). Stained gels were densitometrically analyzed using a FLA-5000 Imager (FUJIFILM) and quantified with the help of FIJI^[59] and Igor Pro 6.37 (Wave Metrics). Further visualization was achieved by atomic force microscopy (AFM). DNA-cholesterol micelles (10 μM monomer concentration) in PBS containing 5 mM MgCl₂ were deposited on freshly cleaved muscovite mica (Plano GmbH) and incubated for 5–10 min at RT. The samples were rinsed with dH₂O and dehydrated in a gentle N₂ stream, however, avoiding complete dryness. Microscopy was performed using a NanoWizard3 Atomic Force Microscope (JPK) equipped with a 160AC-NA (μmasch-Europe) cantilever (ν = 300 kHz, D = 26 N/m). Radial profiles of the micelles were extracted using Gwyddion 2.58^[60] and Gaussian fits of the profiles were used to approximate the full width at half maximum (FWHM).

DNAzyme characterization: DNAzyme-driven cleavage reactions were performed in 50 mM Tris/HCl pH 7.6, 150 mM NaCl at a 5'-FAM-labelled SL-RNA substrate concentration of 5 μM. The RNA was mixed with a 5-fold molar excess of 5'-Cy5-labelled SL-DNAzyme and samples were denatured for 1 min at 75 °C. Formation of the SL-RNA/DNAzyme complex was achieved by cooling to 20 °C at a rate of 0.08 °C/s. Following hybridization, samples were thermally equilibrated at 37 °C and cleavage reactions were started by adding 10 mM MnCl₂. After 30 min, samples were put on ice and supplemented with 50 mM Na₂EDTA pH 8. Reaction products were analyzed in 8 M urea-containing 18% (w/v) polyacrylamide gels and analyzed by fluorescence densitometry using the following wavelength: λ_{ex} 473 nm, λ_{em} LP510 nm, and λ_{ex} 635 nm, λ_{em} LP665). Fluorescence signals were quantified using MultiGauge v3.0 (FUJIFILM). Single-turnover enzyme reactions were performed as above using 2.5 μM 5'-FAM-labelled SL-RNA and a 5-fold molar excess of 3'-cholesterol modified SL-DNAzyme. Samples were incubated at 37 °C in the presence of 10 mM MgCl₂. The divalent cation-dependency of the cleavage reaction was measured at single-turnover conditions in the presence of 10 mM of either BaCl₂, CaCl₂, CoCl₂, CuCl₂, MgCl₂, MnCl₂, NiCl₂, SrCl₂, or ZnCl₂. The pH-optimum was analyzed in 25 mM Tris/HCl between pH 6.8 and pH 8.8. Multiple-turnover kinetics were measured similarly using 15 μM 5'-FAM SL-RNA and 0.5 μM, 1.0 μM, or 1.5 μM 3'-cholesterol modified SL-DNAzyme. The turnover number (k_{cat}) was enumerated from the linear part of the kinetic where ≤30% of the RNA substrate is processed.

Trypanosome growth inhibition: Growth inhibition experiments were performed in 96-well plates using mid- to late-log phase trypanosomes at a cell density of 0.45 × 10⁶/mL. 2 × 10⁴ parasites in 0.05 mL of HMI-9 medium were supplemented with 1–10 μM (monomer concentration) DNA-cholesterol nanoparticles and were grown for 16–46 h at 37 °C. After incubation 5 μM of the cell-permeant compound, Calcein AM (C₃₀H₂₆N₂O₁₃, Life Technologies) was added and the cells were further incubated for 30 min at 37 °C. Cells were pelleted (2000x g, 10 min, 4 °C), washed with ice-cold PBSG (PBS plus 5% (w/v) glucose), and resuspended in 0.2 mL PBSG. Samples were transferred into transparent, flat-bottom 96-well plates and analyzed using a FLA-5000 imager (FUJIFILM) (λ_{ex} 473 nm, λ_{em} 510 nm). Fluorescent signals were quantified using FIJI.^[59] Cells treated with 10% (v/v) EtOH were used for background subtraction and replicates of the background-subtracted samples were averaged and normalized to the maximal signal. LC₅₀-values were calculated as the concentration at 50% fluorescence intensity,

using the built-in sigmoidal fit function of Igor Pro 6.37 (Wave Metrics).

Microscopy and live-cell imaging: Mid-log bloodstream stage trypanosomes were harvested by centrifugation (3000x g, 2 min, RT) and resuspended in HMI-9 medium to a cell density of 0.8×10^6 /mL. The parasites were supplemented with 10 μ M (monomer concentration) DNA-cholesterol nanoparticles and 5 mg/mL fluorescein isothiocyanate (FITC)-dextran with a mean molecular mass of 10 kDa (Sigma-Aldrich) as a fluid phase marker. Cells were grown at 37 °C for 8–16 h followed by pelleting at 2000x g for 5 min at 4 °C. Cells were washed with ice-cold PBSG and fixed with 1% (w/v) paraformaldehyde and 0.08% (w/v) glutaraldehyde in PBS. Fixed cells were supplemented with 1 μ g/mL Hoechst 33258 (C₂₅H₃₇Cl₃N₆O₆, Sigma-Aldrich) and imaged directly or in the presence of 0.5 vol. DABCO antifade (20 mM 1,4-diazabicyclo[2.2.2]octane in 90% (v/v) glycerol). Imaging was performed with a Zeiss Axioskop 2 microscope equipped with a Zeiss Axiocam MRm camera and a Plan Neofluar 100x (NA 1.30) oil-objective. Zeiss filter sets for Hoechst 33258 (λ_{ex} BP365/12, λ_{em} LP397) and FITC/FAM (λ_{ex} BP470/20, λ_{em} BP505-530) were used. Cell shape measurements were made after 8 h of incubation with 10 μ M (monomer concentration) DNA-cholesterol nanoparticles. Cells were fixed and imaged as above, except using a Plan Neofluar 40x air-objective (NA 0.75). Cell diameters were measured using FIJI.^[59] For life-cell imaging, trypanosomes were harvested by centrifugation at 3000x g for 5 min at 4 °C. Cells were resuspended in HMI-9 medium to 5×10^6 cells/mL and supplemented with 20 μ M (monomer concentration) DNA-cholesterol nanoparticles (~500x CMC and 15x LC₅₀). The samples were incubated at 37 °C and aliquots were taken at 4 h, 6 h, 8 h, 10 h, and 14 h and imaged directly using a Plan Neofluar 100x (NA 1.30) oil-objective in DIC-mode using an Axiocam MRm camera at 16 frames/sec. Images were cropped and normalized by dividing the individual frames by the median pixel intensity using FIJI.^[59]

Acknowledgements

The authors thank Michael Brecht and Jacqueline Nentwich for their experimental help at an early stage of the project. Andreas Völker is thanked for maintaining trypanosome cultures and Elisabeth Kruse for discussions. The work was supported by the Illing Foundation for Molecular Chemistry to HUG. Open Access funding enabled and organized by Projekt DEAL.

Conflict of Interest

The authors declare no conflict of interest.

Data Availability Statement

The data that support the findings of this study are available from the corresponding author upon reasonable request.

Keywords: African trypanosomes · chemotherapeutics · DNAzymes · DNA nanoparticles · drug design

- [1] N. Feasey, M. Wansbrough-Jones, D. C. W. Mabey, A. W. Solomon, *Br. Med. Bull.* **2010**, *93*, 179–200.
- [2] D. H. Molyneux, L. Dean, O. Adekeye, J. R. Stothard, S. Theobald, *Parasitology* **2018**, *145*, 1647–1654.
- [3] P. Büscher, G. Cecchi, V. Jamonneau, G. Gerardo Priotto, *Lancet* **2017**, *390*, 2397–2409.
- [4] P. G. E. Kennedy, *J. Neurol.* **2019**, *266*, 2334–2337.
- [5] E. A. Dickie, F. Giordani, M. K. Gould, P. Mäser, C. Burri, J. C. Mottram, S. P. S. Rao, M. P. Barrett, *Trop. Med. Infect. Dis.* **2020**, *5*, 29, <https://doi.org/10.3390/tropicalmed5010029>.
- [6] A. H. Fairlamb, D. Horn, *Trends Parasitol.* **2018**, *34*, 481–492.
- [7] M. P. Pollastri, *Trends Parasitol.* **2018**, *34*, 178–179.
- [8] S. L. Regen, *JACS* **2021**, *1*, 3–7.
- [9] L. Vanhamme, *Infect. Disord.: Drug Targets* **2010**, *10*, 266–282.
- [10] M. Delgado, P. Anderson, J. A. Garcia-Salcedo, M. Caro, E. Gonzalez-Rey, *Cell Death Differ.* **2009**, *16*, 406–416.
- [11] H. X. Koh, H. M. Aye, K. S. W. Tan, C. Y. He, *Microb. Cell Fact.* **2015**, *2*, 288–298.
- [12] S. Alsford, *Microb. Cell Fact.* **2015**, *2*, 259–261.
- [13] W. M. Leeder, F. Giehler, J. Joswig, H. U. Göringer, *ChemBioChem* **2019**, *20*, 1251–1255.
- [14] A. Günzl, *Eukaryotic Cell* **2010**, *9*, 1159–1170.
- [15] H. Goldshmidt, D. Matas, A. Kabi, S. Carmi, R. Hope, S. Michaeli, *PLoS Pathog.* **2010**, *6*, e1000731.
- [16] R. F. S. Menna-Barreto, *Cell Death Dis.* **2019**, *10*, 93.
- [17] A. W. Cornelissen, M. P. Verspiieren, J. J. Toulmé, B. W. Swinkels, P. Borst, *Nucleic Acids Res.* **1986**, *14*, 5605–5614.
- [18] P. Verspiieren, A. W. Cornelissen, N. T. Thuong, C. Hélène, J. J. Toulmé, *Gene* **1987**, *61*, 307–315.
- [19] M. Langecker, V. Arnaut, J. List, F. C. Simmel, *Acc. Chem. Res.* **2014**, *47*, 1807–1815.
- [20] X. Li, K. Feng, L. Li, L. Yang, X. Pan, H. S. Yazd, C. Cui, J. Li, L. Moroz, Y. Sun, B. Wang, X. Li, T. Huang, W. Tan, *Natl. Sci. Rev.* **2020**, *9*, 1933–1953.
- [21] M. Walczak, R. A. Brady, L. Mancini, C. Contini, R. Rubio-Sánchez, W. T. Kauffhold, P. Cicuta, L. Di Michele, *Nat. Commun.* **2021**, *12*, 4743.
- [22] S. Huo, H. Li, A. J. Boersma, A. Herrmann, *Adv. Sci.* **2019**, *6*, 1900043.
- [23] Z. Zhao, Y. Dong, Z. Duan, D. Jin, D. W. Yuan, D. Liu, *Aggregate* **2021**, *2*, e95, <https://doi.org/10.1002/agt2.95>.
- [24] J. K. D. Singh, E. Darley, P. Ridone, J. P. Gaston, A. Abbas, S. F. J. Wickham, M. A. B. Baker, *Nucleic Acids Res.* **2021**, *49*, 10835–10850.
- [25] I. Pfeiffer, F. Höök, *J. Am. Chem. Soc.* **2004**, *126*, 10224–10225.
- [26] A. Bunge, M. Loew, P. Pescador, A. Arbuzova, N. Brodersen, J. Kang, L. Dähne, J. Liebscher, A. Herrmann, G. Stengel, D. Huster, *J. Phys. Chem. B.* **2009**, *113*, 16425–16434.
- [27] P. A. Beales, T. K. Vanderlick, *J. Phys. Chem. B.* **2009**, *113*, 13678–13686.
- [28] P. M. Arnott, H. Joshi, A. Aksimentiev, S. Howorka, *Langmuir* **2018**, *34*, 15084–15092.
- [29] R. P. Cruz, J. B. Withers, Y. Li, *Chem. Biol.* **2004**, *11*, 57–67.
- [30] M. Cepeda-Plaza, A. Peracchi, *Org. Biomol. Chem.* **2020**, *4*, 1697–1709.
- [31] I. N. Kurniasih, H. Liang, P. C. Mohr, G. Khot, J. P. Rabe, A. Mohr, *Langmuir* **2015**, *31*, 2639–2648.
- [32] H. Liu, Z. Zhu, H. Kang, Y. Wu, K. Sefan, W. Tan, *Chem. Eur. J.* **2010**, *22*, 3791–3797.
- [33] Y. Wang, C. Wu, T. Chen, H. Sun, S. Cansiz, L. Zhang, C. Cui, W. Hou, Y. Wu, S. Wan, R. Cai, Y. Liu, B. Sumerlin, X. Zhang, W. Tan, *Chem. Sci.* **2016**, *7*, 6041–6049.
- [34] J. Zou, C. Jin, R. Wang, H. Kuai, L. Zhang, X. Zhang, J. Li, L. Qiu, W. Tan, *Anal. Chem.* **2018**, *90*, 6843–6850.
- [35] H. Yin, H. Wang, Z. Li, D. Shu, P. Guo, *ACS Nano.* **2019**, *13*, 706–717.
- [36] C. J. Kim, G. H. Kim, E. H. Jeong, H. Lee, S. J. Park, *Nanoscale* **2021**, *28*, 13758–13763.
- [37] S. A. Weston, C. R. Parish, *J. Immunol. Methods* **1990**, *133*, 87–97.
- [38] D. Bratosin, L. Mitrofan, C. Paliu, J. Estaquier, J. Montreuil, *Cytometry Part A* **2005**, *66*, 78–84.
- [39] H. Y. Saad, W. I. Higuchi, *J. Pharm. Sci.* **1965**, *54*, 1205–1206.
- [40] S. Ohkuma, Y. Moriyama, T. Takano, *Proc. Natl. Acad. Sci. USA* **1982**, *79*, 2758–2762.
- [41] H. P. De Koning, D. J. Bridges, R. J. Burchmore, *FEMS Microbiol. Rev.* **2005**, *29*, 987–1020.
- [42] G. D. Campagnaro, K. J. Alzahrani, J. C. Munday, H. P. De Koning, *Mol. Biochem. Parasitol.* **2018**, *220*, 46–56.
- [43] M. Homann, H. U. Göringer, *Nucleic Acids Res.* **1999**, *1*, 2006–2014.
- [44] M. Homann, H. U. Göringer, *Bioorg. Med. Chem.* **2001**, *9*, 2571–2580.
- [45] A. Adler, N. Forster, M. Homann, H. U. Göringer, *Comb. Chem. High Throughput Screening* **2008**, *11*, 16–23.

- [46] M. Engstler, L. Thilo, F. Weise, C. G. Grünfelder, H. Schwarz, M. Boshart, P. Overath, *J. Cell Sci.* **2004**, *117*, 1105–1115.
- [47] J. J. McManus, J. O. Rädler, K. A. Dawson, *J. Phys. Chem. B* **2003**, *107*, 9869–9875.
- [48] A. Michanek, N. Kristen, F. Höök, T. Nylander, E. Sparr, *Biochim. Biophys. Acta.* **2010**, *1798*, 829–838.
- [49] D. Morzy, R. Rubio-Sánchez, H. Joshi, A. Aksimentiev, L. Di Michele, U. F. Keyser, *J. Am. Chem. Soc.* **2021**, *143*, 7358–7367.
- [50] R. S. Gracià, N. K. Bezlyepkina, R. L. Knorr, R. Lipowsky, R. Dimova, *Soft Matter* **2010**, *6*, 1472–1482.
- [51] W. K. Subczynski, M. Pasenkiewicz-Gierula, J. Widomska, L. Mainali, M. Raguz, *Cell Biochem. Biophys.* **2017**, *75*, 369–385.
- [52] S. Chakraborty, M. Doktorova, T. R. Molugu, F. A. Heberle, H. L. Scott, B. Dzikovski, M. Nagao, L. R. Stingaciu, R. F. Standaert, F. N. Barrera, J. Katsaras, G. Khelashvili, M. F. Brown, R. Ashkar, *Proc. Natl. Acad. Sci. USA* **2020**, *117*, 21896–21905.
- [53] A. Biswas, P. Kashyap, S. Datta, T. Sengupta, B. Sinha, *Biophys. J.* **2019**, *116*, 1456–1468.
- [54] F. Zakany, T. Kovacs, G. Panyí, Z. Varga, *Biochim. Biophys. Acta Mol. Cell Biol. Lipids* **2020**, *1865*, 158706.
- [55] A. Vanhollebeke, L. Lecordier, D. Perez-Morga, A. Amiguet-Vercher, *J. Eukaryotic Microbiol.* **2007**, *54*, 448–451.
- [56] G. Vanwallegghem, F. Fontaine, L. Lecordier, P. Tebabi, K. Klewe, D. P. Nolan, Y. Yamaryo-Botté, C. Botté, A. Kremer, G. S. Burkard, J. Rassow, I. Roditi, D. Pérez-Morga, E. Pays, *Nat. Commun.* **2015**, *6*, 8078.
- [57] H. Hirumi, K. Hirumi, *J. Parasitol.* **1989**, *75*, 985–989.
- [58] R. Brun, M. Schönenberger, *Acta Trop.* **1979**, *36*, 289–292.
- [59] J. Schindelin, I. Arganda-Carreras, E. Frise, V. Kaynig, M. Longair, T. Pietzsch, S. Preibisch, C. Rueden, S. Saalfeld, B. Schmid, J. Y. Tinevez, D. J. White, V. Hartenstein, K. Eliceiri, P. Tomancak, A. Cardona, *Nat. Methods* **2012**, *9*, 676–682.
- [60] D. Nečas, P. Klapetek, *Open Phys.* **2012**, *10*, 181–188.

Manuscript received: July 20, 2022

Revised manuscript received: August 18, 2022

Accepted manuscript online: August 30, 2022

Version of record online: September 20, 2022